

# Is Pre-training Applicable to the Decoder for Dense Prediction?

Chao Ning  
The University of Tokyo

Wanshui Gan  
The University of Tokyo

Weihaio Xuan  
The University of Tokyo

Naoto Yokoya  
The University of Tokyo

## Abstract

Encoder-decoder networks are commonly used model architectures for dense prediction tasks, where the encoder typically employs a model pre-trained on upstream tasks, while the decoder is often either randomly initialized or pre-trained on other tasks. In this paper, we introduce  $\times$ Net, a novel framework that leverages a model pre-trained on upstream tasks as the decoder, fostering a “pre-trained encoder  $\times$  pre-trained decoder” collaboration within the encoder-decoder network.  $\times$ Net effectively addresses the challenges associated with using pre-trained models in the decoding, applying the learned representations to enhance the decoding process. This enables the model to achieve more precise and high-quality dense predictions. By simply coupling the pre-trained encoder and pre-trained decoder,  $\times$ Net distinguishes itself as a highly promising approach. Remarkably, it achieves this without relying on decoding-specific structures or task-specific algorithms. Despite its streamlined design,  $\times$ Net outperforms advanced methods in tasks such as monocular depth estimation and semantic segmentation, achieving state-of-the-art performance particularly in monocular depth estimation.

## 1. Introduction

Since 2015, Jonathan et al. [35] have reinterpreted classification networks as fully convolutional architectures, fine-tuning these models based on their pre-learned representations. Pre-trained models excel at extracting features across multiple scales, from fine to coarse, effectively capturing both local and global information from images.

In the years that followed, numerous studies have explored improved network structures to decode these visual features, establishing end-to-end networks that provide effective solutions for various dense prediction tasks such as monocular depth estimation [3, 17, 26, 42], semantic segmentation [30, 52, 61], and optical flow estima-

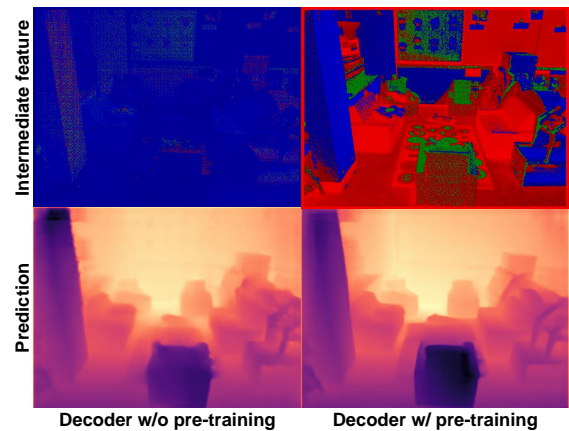


Figure 1. Comparison of pre-trained and non-pre-trained decoders. When paired with a consistent encoder and architecture, a pre-trained decoder enhances the semantic richness of encoded feature maps and refines the final predictions.

tion [36, 50, 54]. In these tasks, pre-trained models act as encoders to extract features, which are progressively refined from coarse visual representations to pixel-level predictions through randomly initialized decoding techniques.

Recently, networks trained with larger datasets have emerged as promising solutions for a variety of computer vision tasks, including image classification [48], self-supervised learning [37], semantic segmentation [25], and depth prediction [20, 55]. The expansion of training data has resulted in significant enhancements in network performance, enabling classical network structures to surpass even more advanced architectures. For example, in the field of monocular depth estimation, Depth Anything [55] employs the 2021 architecture of DPT [40], trained with larger datasets, and is able to surpass the state-of-the-art architectures of 2023, such as NDDepth [42].

Reflecting on encoder-decoder networks for dense prediction, the encoder is typically a pre-trained model, while

the decoder is usually initialized randomly. This raises an important question: given that increased training data can enhance network performance, why is the decoder not pre-trained as well?

To address this, we investigate why encoders benefit from pre-training to improve performance, whereas decoders typically do not.

To use a pre-trained model as a decoder, two important challenges must be addressed. First, (1) the decoder’s structure inherently differs from that of the pre-trained model, preventing it from loading pre-trained parameters. Second, (2) as the decoding component, the decoder must derive dense predictions from features, which differs from the encoder’s goal of extracting features from images. Therefore, the parameters pre-trained on upstream tasks may not necessarily be suitable for decoding.

In this paper, we introduce  $\times$ Net, which facilitates a “pre-trained encoder  $\times$  pre-trained decoder” collaboration. It addresses the challenges of using a pre-trained model as a decoder, enabling pre-learned knowledge to be utilized in the decoder of a dense prediction network, thereby achieving significant improvements. As shown in Figure 1,  $\times$ Net enriches the network’s intermediate feature maps with semantic information. This semantic information, which is not supervised during dense prediction tasks, can only be acquired through pre-training and aids in achieving higher-quality dense predictions. When magnified, it is clearly observable that the pre-trained decoder exhibits sharper edges and finer details.

In summary, our core contributions are as follows:

- To the best of our knowledge, we are the first to propose applying a pre-trained model as a decoder in dense prediction network and to address the challenges associated with using pre-trained models in the decoding.
- We explored why a pretrained decoder is necessary for dense prediction, emphasizing its ability to provide semantic information crucial for achieving high-quality outputs.
- Extensive experiments demonstrate that using a pre-trained decoder, without additional complex task-specific designs, can achieve advanced performance.

## 2. Related work

### 2.1. Model pre-training

Model pre-training facilitates the learning of visual representations, improving the performance of vision models in downstream tasks. Supervised training for image classification is a classical and widely utilized pre-training method, with classification accuracy serving as an evaluative metric for model performance. ImageNet-1k [41] training, which includes 1.28 million training images across one thousand categories, is a standard regimen. To enable networks to

learn richer visual representations, image classification with more categories and a greater number of images is employed in pre-training. To effectively enhance the quality of pre-training, methods such as BEiT [2], which utilize masked image modeling, CLIP [39], which employs image-language data pairs for classification training, and DINO [5, 37], which focus on self-supervised learning for vision transformers, leverage extensive datasets to make the models more robust. Previously, these pre-trained networks could only serve as encoders in dense prediction networks for feature extraction. In this paper, we are the first to utilize these networks as decoders to decode encoded features.

### 2.2. Encoder-decoder networks for dense prediction

The pioneering work [35] first employed a decode head to fine-tune networks that achieved success in image benchmarks, specifically for pixel-level semantic segmentation. This innovative approach inspired the advancement of numerous dense prediction tasks, which now focus on the efficient decoding of features extracted by pre-trained encoders. To effectively capture multi-scale information, Feature Pyramid Networks (FPN) [24, 31] incorporate encoded features at various resolutions into the decoding process. This straightforward yet effective concept has become a fundamental architecture widely adopted in dense prediction networks. Based on the FPN architecture, some works enhance network performance by improving network structures. These improvements include plug-in modules [8, 21, 49, 61], decoding architecture [40] adapted to columnar Vision Transformer (ViT) encoders, and decoders utilizing transformer architectures [10, 11, 28, 57]. On the other hand, the dense prediction performance is improved through specialized algorithms tailored to specific tasks. For instance, customized context [6, 7, 60] in semantic segmentation, clustering algorithms [9, 23] in instance segmentation, bins classification [3, 4, 43], normal distance assistance [42], and ground embedding [56] in monocular depth estimation. Our experiments demonstrate that introducing a pre-trained decoder can surpass advanced decoding structures and specialized algorithms.

## 3. From pre-trained model to decoder

In this section, we investigate how to effectively integrate pre-trained model into the decoder, addressing two major challenges. First, common dense prediction network decoders cannot utilize pre-trained parameters. Second, even if pre-trained parameters can be loaded into the decoder, ensuring effective use of the pre-learned representations during the decoding process remains a challenge. We conduct a theoretical analysis of these two challenges, propose solutions, and finally summarize our method, introducing  $\times$ Net, a dense prediction network that efficiently leverages a pre-trained decoder. We select the widely utilized hier-

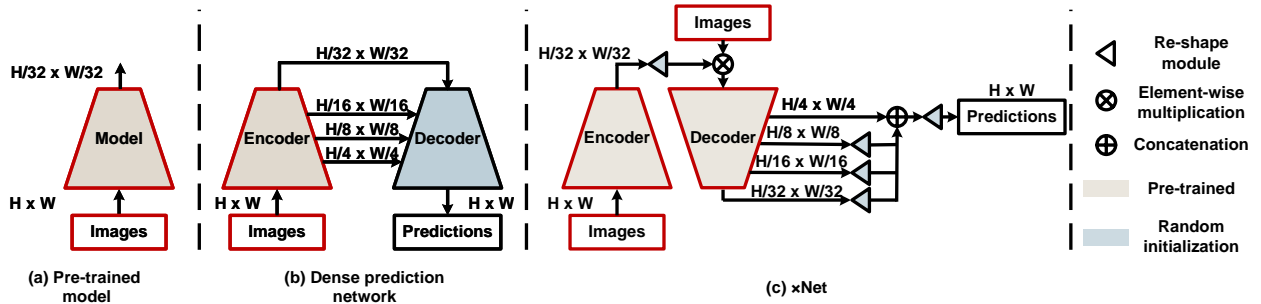


Figure 2. Overview of the image classification model (left), encoder-decoder network (middle), and our  $\times$ Net (right). The pre-trained model represents the commonly used hierarchical structure.

archical model pre-trained on image classification tasks to represent the pre-trained models. Additionally, we employ an encoder-decoder network with hierarchically connected pyramidal structures to represent common dense prediction networks.

### 3.1. Why pre-training is not available for decoder?

**Reversed structure.** As illustrated in Figure 2, the primary reason pre-training is not applied to decoders is that the structure of decoders is reversed compared to that of pre-trained models. Pre-trained models typically reduce the spatial size of features progressively to extract image categories, whereas dense prediction requires reconstructing high-resolution pixel-level predictions from low-resolution feature maps. The resolutions of feature maps in traditional decoders and pre-trained models can be described as follows:

$$\left\{ \begin{array}{l} F^{\frac{1}{32}} \xrightarrow{\mathcal{D}_1} F^{\frac{1}{16}} \xrightarrow{\mathcal{D}_2} F^{\frac{1}{8}} \xrightarrow{\mathcal{D}_3} F^{\frac{1}{4}} \xrightarrow{\mathcal{D}_4, \text{head}} F^1 \\ F^1 \xrightarrow{\text{stem}, \mathcal{P}_1} F^{\frac{1}{4}} \xrightarrow{\mathcal{P}_2} F^{\frac{1}{8}} \xrightarrow{\mathcal{P}_3} F^{\frac{1}{16}} \xrightarrow{\mathcal{P}_4} F^{\frac{1}{32}} \end{array} \right. \quad (1)$$

Here,  $\mathcal{D}$  and  $\mathcal{P}$  denote the stages of the decoder and the pre-trained model, respectively, with the subscript indicating their sequential order within the model.  $F$  represents the feature map, and the superscript denotes the downsampling factor of the width and height. The reversed decoding structure is a prerequisite for utilizing pre-trained parameters. Obviously, employing a pre-trained decoder requires input features at the original resolution and output pixel-level predictions.

**Reversed decoder input.** As described in Equation 1, the input to the decoder is  $F^{\frac{1}{32}}$ , which must be reshaped to an appropriate resolution, such as  $F^1$ , to be compatible with the pre-trained decoder. We propose a Re-Shape (RS) module to directly re-shape the encoded feature maps to high resolution for reversed decoder structure. We propose a simple Re-Shape (RS) module that directly reshapes the encoder output to a size suitable for input into the reversed

decoder structure. Specifically, the RS module consists of a normalization layer and a two-layer MLP, with upsampling achieved through a PixelShuffle [44] module positioned of the MLP.

**Reversed decoder prediction.** According to Equation 1, the traditional decoder is required to produce pixel-level predictions ( $F^1$ ). Achieving pixel-level predictions directly from the output of a pre-trained model ( $F^{\frac{1}{32}}$ ) is challenging. Therefore, we propose the Post Feature Pyramid (PFP), which reshapes the feature maps from each of the four stages of the pre-trained decoder to the same resolution using the RS module. These reshaped features are then concatenated along the channel dimension and subsequently fused through another RS module.

With the aforementioned adjustments, the pre-trained model can be used as a decoder, enabling pixel-level predictions in dense prediction tasks.

### 3.2. How to fine-tune pre-trained decoder?

**Optimization challenges.** To effectively fine-tune a pre-trained decoder and fully leverage its learned representations during decoding, it is important to mitigate the optimization challenges. As illustrated in Figure 2, decoders in common dense networks are required to process features from multiple stages of the encoder’s output. In contrast, pre-training typically involves extracting features and recognizing objects from image inputs. Thus, to facilitate optimization, decoding should be aligned in a manner that complements the pre-learned representations.

**Optimization of decoder stages.** In dense prediction networks, the pyramidal connections between the encoder and decoder can introduce optimization difficulties for the pre-trained decoder. The traditional feature pyramid structure can be defined as follows:

$$F^{\frac{1}{k}} = D_i(E_i^{\frac{1}{k}} + D_{i-1}(F^{\frac{1}{2k}})), 2 \leq i \leq 4. \quad (2)$$

Here  $D_i$  is the  $i$ th decoder stage,  $F$  denotes the feature map of the decoder,  $E_i$  is encoded feature map for  $i$ th decoder

stage and  $\frac{1}{k}$  denotes a down-sampling factor of the width and height. Consider  $E_i$  input into pre-trained  $D_i$  as follows:

$$E_i = \phi_i(X_i), \quad (3)$$

where  $\phi_i$  represents the variation from the pre-learned representation  $X_i$ . For each  $D_i$ , there is a variation as follows:

$$\Delta_i = \|D_i(E_i) - D_i(X_i)\|^2, \quad (4)$$

For  $D_2, D_3$ , and  $D_4$ , optimization can be approximately defined as:

$$\min_{D_i} \|D_i(E_i) - D_i(X_i)\|^2 + \|D_i(\Delta_{i-1})\|^2. \quad (5)$$

Here the input  $E_i$  of FP introduces an additional term to the optimization objective ( $\|D_i(E_i) - D_i(X_i)\|^2$ ). Hence, we remove the FP structure for eliminating the optimization of  $\|D_i(E_i) - D_i(X_i)\|^2$ .

**Optimization of decoder input.** According to Equation 3, the variation of decoder input can be defined as:

$$\phi(I) = \hat{E}(I), \quad (6)$$

where  $I$  denotes the input image, and  $\hat{E}$  is the encoder. Then the optimization target can be approximately described as follows:

$$\begin{cases} \min_{D_1} \|D_1(\hat{E}(I)) - D_1(I)\|^2 \\ \min_{D_i} \|D_i(\Delta_{i-1})\|^2, 2 \leq i \leq 4 \end{cases}. \quad (7)$$

The key to reducing optimization difficulty lies in ensuring that  $D_i$  processes encoded features in a manner consistent with image processing. For instance, if at a certain stage the decoding of encoded features is equivalent to processing the image, subsequent stages can align with the pre-trained representations without further optimization. However, retrieving image information from encoded features is challenging, as the encoder’s output is abstract and not a simple transformation of the image. Therefore, we mix the input to the pre-trained decoder with the original image, integrating it into the features through element-wise multiplication. This allows  $\hat{E}(I)$  to be considered a transformation of  $I$ , and optimization can progress along the trajectory of this transformation.

With these designs, the decoding process more closely mirrors the image processing of pre-training, reducing the difficulty of optimization and facilitating the transfer of pre-learned representations to the decoding.

### 3.3. Dense prediction using pre-trained decoder

In this subsection, we summarize the solutions to the challenges faced by pre-trained decoders in dense prediction and introduce  $\times$ Net, a network capable of performing dense prediction with a “pre-trained Encoder  $\times$  pre-trained Decoder” architecture. As illustrated in Figure 2, compared

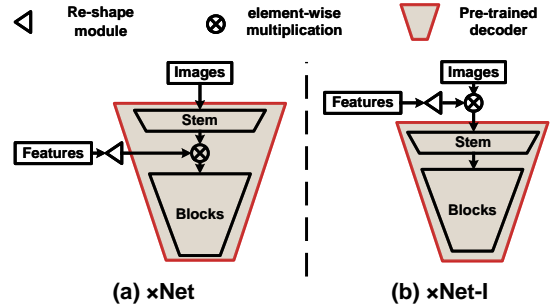


Figure 3. The difference between  $\times$ Net and  $\times$ Net-I.

to conventional dense networks,  $\times$ Net features a reversed decoder and employs a PFP to achieve pixel-level predictions. By removing the pyramidal connections between the encoder and decoder and integrating image data into the encoded features, the pre-trained representations are more effectively incorporated into the decoding process. The red-highlighted parts in Figure 2 clearly show that  $\times$ Net’s encoder-decoder structure and workflow closely resemble that of the pre-trained model. For the method of mixing encoded features into image processing, we propose two approaches, as illustrated in Figure 3. The first approach, used in  $\times$ Net, mixes the encoded features with the output of the stem. The second approach, applied in  $\times$ Net-I, mixes the encoded features directly with the RGB image. The mixing method of  $\times$ Net-I provides an intuitive visualization analysis strategy; however, since it compresses the encoded features to a smaller size (approximately  $\frac{1}{4}$  to  $\frac{1}{2}$ ) of the pixel count of the stem features, hence its performance is slightly inferior to that of  $\times$ Net.

## 4. Experiment settings

In this section, we present the dense prediction tasks discussed in this paper, the datasets employed, and the experimental setup.

### 4.1. Dense prediction tasks

Similar to previous works [22, 40] on dense prediction, we select two popular dense prediction tasks: monocular depth estimation (MDE) and semantic segmentation.

**MDE.** MDE is a pixel-level regression task that involves predicting 3D depth information from a single 2D image. The widely used approach for this task employs a pre-trained encoder to extract features from the image, followed by a decoder module, which is randomly initialized, to decode depth information from the extracted features. Recent methods achieve improved depth prediction by designing advanced model architectures, while others use camera parameters to derive geometric information from images to

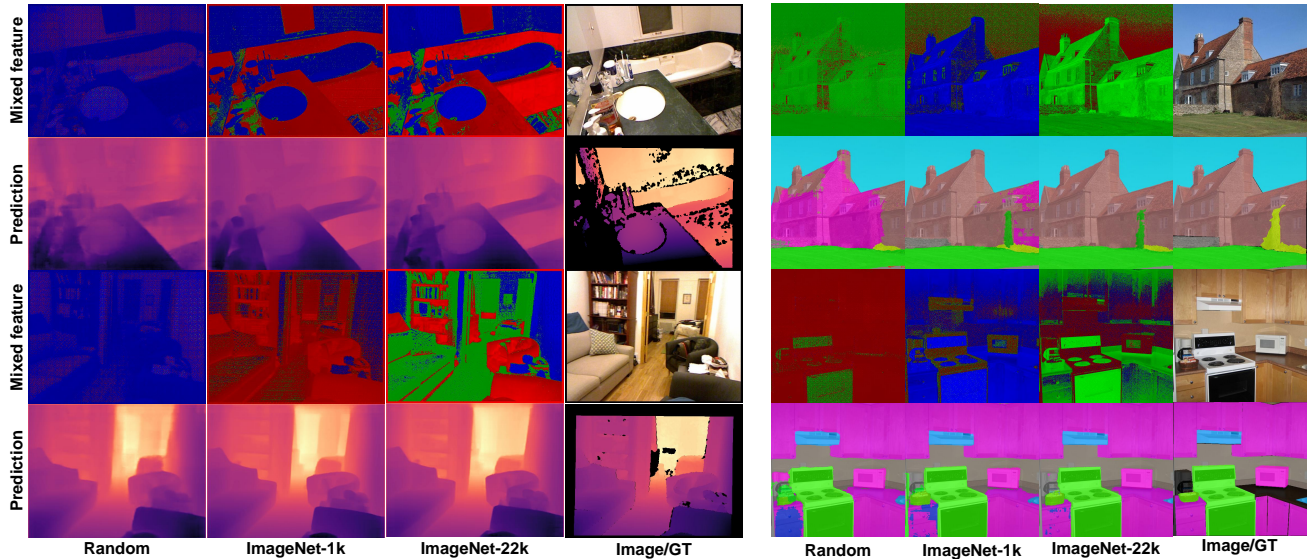


Figure 4. Qualitative comparisons of decoder pre-training on monocular depth estimation (left) and semantic segmentation (right). For mixed feature visualization, extract the maximum value from the RGB components, setting the remaining values to zero.

assist in more accurate depth regression.

**Semantic segmentation.** Semantic segmentation is a pixel-level classification task that requires predicting the precise category for each pixel. Due to the potentially large differences in target sizes, typical semantic segmentation methods utilize a multi-branch decoding structure to capture richer contextual information, enabling accurate classification for each pixel.

## 4.2. Datasets and settings

To comprehensively evaluate our approach, we conducted experiments on four monocular depth estimation (MDE) datasets and two semantic segmentation datasets.

**MDE settings.** We conducted training on three classic monocular depth estimation datasets: NYU-Depth-V2 [45], KITTI [16], and DDAD [19], using the same training and validation splits as the comparison methods. Additionally, following previous works [3, 42, 58], the model trained on the indoor dataset NYU-Depth-V2 is subjected to zero-shot validation on another indoor dataset, SUN RGB-D [46]. We follow the data preprocessing described in [28] for the NYU-Depth-V2 and KITTI datasets, and follow the procedures outlined in [56] for the DDAD dataset. In NYU-Depth-V2, KITTI, and DDAD datasets, the maximum depth is capped at 10m, 80m, and 200m, respectively.

**Semantic segmentation settings.** We performed semantic segmentation experiments on the ADE20K [63] dataset, which contains 150 categories, and the Cityscapes [13] dataset, comprising 19 categories. Following previous work [33], we use the mmsegmentation toolbox [12] for standard training. The crop size for ADE20K is  $512 \times 512$ ,

and for Cityscapes, it is  $512 \times 1024$ .

## 5. Role of pre-trained decoders

In this section, we first conduct ablation experiments on  $\times$ Net to evaluate the impact of each design component on the model’s performance. We then use  $\times$ Net-I to analyze how the pre-trained decoder contributes to performance improvements in dense prediction tasks. All encoders are ImageNet-22k pre-trained ConvNeXt-T [34], and all decoders are ConvNeXt-T based structures.

### 5.1. Ablation study

In this subsection, we progressively modify an FPN into  $\times$ Net, with the results presented in the first group of Table 1. As shown in the first row of Table 1, the ConvNeXt-T structure is not well-suited for dense prediction decoding. Reversing the decoding structure (from high resolution to low resolution) results in a slight improvement in MDE but a decrease in performance in semantic segmentation. Once the decoding structure is reversed, pre-trained parameters can be loaded into the decoder. Using ImageNet-22k pre-training in the decoder significantly enhances model performance (reducing Abs Rel by 4.81% and improving mIoU by 4.78%). Adding PFP and removing FP yield slight improvement. Mixing feature maps into image processing aids the transfer of pre-learned representations to the decoder: the mixing method of  $\times$ Net-I reduces Abs Rel by 2.04% and improve mIoU by 1.01%, while the mixing method of  $\times$ Net reduces Abs Rel by 3.06% and improve mIoU by 1.26%.

In summary, it is evident that the pre-trained decoder

Variant	NYU MDE		ADE20k Seg.	
	$\delta < 1.25 \uparrow$	Abs Rel $\downarrow$	mAcc $\uparrow$	mIoU $\uparrow$
FPN	0.889	0.106	52.92	42.82
+Rev.	0.896	0.104	52.42	42.31
+22k	0.909	0.099	55.32	44.71
+PFP	0.910	0.098	55.47	44.82
-FP	0.911	0.098	55.97	45.34
$\times$ Net-I-22k	0.912	0.096	56.57	45.80
$\times$ Net-22k	0.916	0.095	56.82	45.91
$\times$ Net-I-0	0.899	0.104	52.72	42.67
$\times$ Net-I-1k	0.908	0.100	55.50	44.83
$\times$ Net-I-22k	0.912	0.096	56.57	45.80

Table 1. Ablation study and pre-training comparisons on NYU-Depth-V2 MDE and ADE20k semantic segmentation. The first group is the ablation study result. The second group involves comparisons among various decoders based on their pre-training volumes. Specifically, “0” indicates no pre-training, while “1k” and “22k” refer to pre-training on ImageNet-1k and ImageNet-22k, respectively.

stands as a pivotal element in the architectural design of  $\times$ Net. Consequently, the next subsection will delve into an analysis of the mechanisms through which the pre-trained decoder enhances the efficacy of  $\times$ Net.

## 5.2. Why decoder require pre-training?

In this subsection, we utilize  $\times$ Net-I to investigate the role of pre-trained decoders on network performance. We conduct both quantitative and qualitative analyses. We compare same decoder with different initializations: randomly initialized, pre-trained on ImageNet-1k classification, and pre-trained on ImageNet-22k classification.

**Quantitative analyse.** As shown in the second group of Table 1, compared to the non-pre-trained decoder, the ImageNet-1k pre-trained decoder achieves a 4.84% reduction in Abs Rel, along with improvements of 5.27% in mAcc and 5.06% in mIoU. In contrast, the ImageNet-22k pre-trained decoder demonstrates significant enhancements, with a 7.69% reduction in Abs Rel and improvements of 7.30% in mAcc and 7.34% in mIoU.

**Quantitative analyses.** For quantitative analyses, we visualize the mixed features and the final predictions. For  $\times$ Net-I, due to its mixed feature being a three-channel feature map integrated into the RGB image, it inherently provides a visualization advantage.

The qualitative comparisons are shown in Figure 4. There is an interesting observation: despite utilizing the same encoder, differences in the pre-training of the decoder resulted in significant variations in the mixed features. It is evident that the features of the decoder without pre-training are mostly concentrated in the same chan-

nels, whereas the pre-trained decoder allows for the observation of semantic information in the mixed feature. As explained in Subsection 3.2,  $\times$ Net-I aligns the optimization of pre-trained decoder closely with image processing. As a result, the pre-learned representations in the decoder are effectively transferred into the decoding process. For instance, the sofa in the third row of the MDE as shown in Figure 4 is well-separated into channels distinct from surrounding objects. This separation is more pronounced with the ImageNet-22k pre-trained decoder compared to the ImageNet-1k pre-trained decoder, indicating higher confidence with ImageNet-22k pre-training. Given that MDE supervises the depth prediction and the model cannot gain semantic information from MDE training. Such clustering of semantic information can only be derived from the knowledge gained during pre-training.

As illustrated by the prediction comparisons in Figure 4, the inclusion of semantic information in the mixed feature contributes to improvements beyond mere accuracy. In MDE predictions, decoders without pre-training produce coarser outputs, where noticeable jagged edges can be observed upon magnification. In contrast, predictions from pre-trained decoders exhibit sharper details. For semantic segmentation, there is a more coherent output with pre-trained decoders, whereas decoders without pre-training tend to predict different categories within the same object. Pre-trained decoders significantly mitigate this issue. The semantic information embedded in the mixed feature enables the decoding process to effectively leverage pre-learned representations for improved prediction.

It can be concluded that pre-trained knowledge is effectively transferable to the decoder, endowing the network’s mixed features with semantic information. This semantic enrichment can be leveraged in dense prediction tasks to provide sharper details and more coherent predictions.

## 6. Dense prediction performances

In this section, we compare  $\times$ Net with other advanced methods. To thoroughly evaluate the advantages of the pre-trained decoder, **we do not incorporate task-specific designs in  $\times$ Net**. Instead, we employed a simple linear probe for prediction. To ensure a fair comparison, we use the same encoder as the main competing methods, including identical model architecture and encoder pre-training. Training was conducted using only standard data augmentation without introducing additional strategies. Moreover, we strictly controlled the computational cost of  $\times$ Net using FPS as a metric, ensuring that performance improvements are entirely due to the advantages of the pre-trained decoder.

### 6.1. Quantitative comparisons

**NYU-Depth-V2 and KITTI results.** Table 2 and Table 3 compare the monocular depth estimation results of

Method	Backbone	$\delta < 1.25 \uparrow$	Abs Rel $\downarrow$	log10 $\downarrow$
DepthFormer [27]	Swin-L [33]	0.921	0.096	0.041
NeW CRFs [58]	Swin-L [33]	0.922	0.095	0.041
BinsFormer [28]	Swin-L [33]	0.925	0.094	0.040
PixelFormer [1]	Swin-L [33]	0.929	0.090	0.039
MG [32]	Swin-L [33]	0.933	0.087	-
NDDepth [42]	Swin-L [33]	<b>0.936</b>	0.087	0.038
$\times$ ConvNeXtV2-T (ours)	Swin-L [33]	<b>0.936</b>	<b>0.086</b>	<b>0.037</b>
Depth Anything [55]	DINOv2-L [37]	0.984	0.056	0.024
Metric3Dv2 [20]	DINOv2-L [37]	0.989	0.047	<b>0.020</b>
$\times$ ConvNeXtV2-B (ours)	DINOv2-L [37]	<b>0.990</b>	<b>0.045</b>	<b>0.020</b>

Table 2. MDE results on the NYU-Depth-V2 dataset.

Method	Backbone	$\delta < 1.25 \uparrow$	Abs Rel $\downarrow$	RMS_log $\downarrow$
NeW CRFs [58]	Swin-L [33]	0.974	0.052	0.079
BinsFormer [28]	Swin-L [33]	0.974	0.052	0.079
DepthFormer [27]	Swin-L [33]	0.975	0.052	0.079
PixelFormer [1]	Swin-L [33]	0.976	0.051	0.077
MG [32]	Swin-L [33]	0.976	0.050	<b>0.075</b>
NDDepth [42]	Swin-L [33]	<b>0.978</b>	0.050	<b>0.075</b>
$\times$ ConvNeXt-B (ours)	Swin-L [33]	<b>0.978</b>	<b>0.048</b>	<b>0.075</b>
Depth Anything* [55]	DINOv2-L [37]	0.982	0.046	0.069
Metric3Dv2* [20]	DINOv2-L [37]	0.985	0.044	0.060
$\times$ ConvNeXtV2-B (ours)	DINOv2-L [37]	<b>0.988</b>	<b>0.037</b>	<b>0.056</b>

Table 3. MDE results on the KITTI dataset.

Method	Backbone	$\delta < 1.25 \uparrow$	Abs Rel $\downarrow$	log10 $\downarrow$
BinsFormer [28]	Swin-L [33]	0.805	0.143	0.061
PixelFormer [1]	Swin-L [33]	0.802	0.144	0.062
DepthFormer [27]	Swin-L [33]	0.815	0.137	0.060
NDDepth [42]	Swin-L [33]	0.820	0.137	0.060
$\times$ ConvNeXtV2-T (ours)	Swin-L [33]	<b>0.824</b>	<b>0.133</b>	<b>0.059</b>

Table 4. Zero-shot performances on the SUN RGB-D dataset.

$\times$ Net with methods specifically designed for monocular depth estimation, and  $\times$ Net shows state-of-the-art performance. With the same Swin-L backbone, it surpasses ND-Depth on both the NYU-Depth-V2 dataset (0.086 Abs Rel vs. 0.087 Abs Rel) and the KITTI dataset (0.048 Abs Rel vs. 0.050 Abs Rel). Unlike NDDepth, which requires using camera intrinsics to compute Normal-Distance for depth prediction, our method simply employs a pre-trained ConvNeXtV2-T [51] or ConvNeXt-B [34] for decoding. For the Metric3Dv2 [20] trained on large-scale datasets, we achieve significant improvements over Metric3Dv2’s fine-tuning results on the KITTI dataset (0.037 Abs Rel vs. 0.044 Abs Rel) using Metric3Dv2 pre-trained DINOv2  $\times$  ConvNeXtV2-B [51].

**Zero-shot results of SUN RGB-D and online evaluation on KITTI server.** Following previous works [1, 27, 28, 42], we evaluate the NYU-Depth-V2 trained model on the SUN RGB-D dataset. The results in Table 4 show that our pre-trained ConvNeXtV2-T decoder achieved the best generalization performance, surpassing previous methods across all three metrics. Additionally, we uploaded the

Method	SILog $\downarrow$	sqRel $\downarrow$	absRel $\downarrow$	iRMSE $\downarrow$
NeW CRFs [58]	10.39	1.83	8.37	11.03
PixelFormer [28]	10.28	1.82	8.16	10.84
BinsFormer [28]	10.14	1.69	8.23	10.90
DepthFormer [28]	10.69	1.84	8.68	11.39
MG [32]	9.93	1.68	7.99	10.63
NDDepth [42]	9.62	1.59	7.75	10.62
UniDepth [38]	8.13	1.09	6.54	8.24
D2L $\times$ C2B	<b>7.51</b>	<b>0.93</b>	<b>6.14</b>	<b>7.62</b>

Table 5. MDE performances on the online KITTI evaluation server. “D2L $\times$ C2B” denotes DINOv2-L encoder  $\times$  ConvNeXtV2-B decoder.

Method	Backbone	Abs Rel $\downarrow$	Sq Rel $\downarrow$	RMS_log $\downarrow$
DepthFormer [27]	Swin-L [33]	0.152	2.230	0.246
PixelFormer [1]	Swin-L [33]	0.151	2.140	0.242
BinsFormer [28]	Swin-L [33]	0.149	2.142	0.244
DepthFormer(GEV) $\dagger$ [56]	Swin-L [33]	0.149	2.121	0.240
DepthFormer(GEA) $\dagger$ [56]	Swin-L [33]	0.145	2.119	0.237
$\times$ ConvNeXt-B (ours)	Swin-L [33]	<b>0.144</b>	<b>2.116</b>	<b>0.235</b>

Table 6. MDE performances on the DDAD dataset. Methods using extra camera parameter inputs are marked with “ $\dagger$ ”.

KITTI benchmark training results to the KITTI server for validation. At the time of submission, our model **ranked 1st** among all submissions. As shown in Table 3, our method significantly outperforms the previous state-of-the-art method [38] across all four metrics.

**DDAD results.** Table 6 presents the results on the DDAD dataset.  $\times$ Net significantly outperforms many representative models [1, 27, 28]. Furthermore, even when DepthFormer incorporates ground embedding [56], which requires extra camera parameter inputs, our model achieves better results with a simple combination of Swin-L  $\times$  ConvNeXt-B.

**ADE20K results.** Table 7 presents the comparison results on the ADE20K dataset, where our combination of Swin-L $\times$ ConvNeXt-L achieved the best results. Using only a 512 $\times$ 512 crop size, we surpassed UperNet trained with a 640 $\times$ 640 crop size using Swin-L, ConvNeXt-L, and ConvNeXt-XL backbones. Additionally, this simple combination also outperformed the 3-step diffusion model, DDP [22].

**Cityscapes results.** As shown in Table 8,  $\times$ Net surpasses various specialized semantic segmentation methods on the Cityscapes dataset. By using ConvNeXt-L for decoding, it exceeds the performance of Mask2Former [11] (83.63 mIoU vs. 83.30 mIoU), even when Mask2Former employs a dual decoder structure with pixel and Transformer decoders and is trained with additional loss functions, all while using the same backbone.

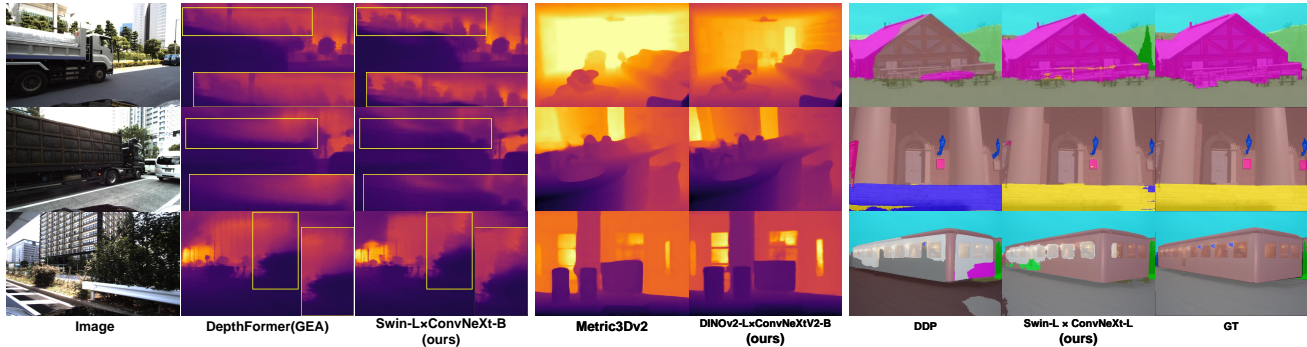


Figure 5. Qualitative comparisons on DDAD MDE (left) and NYU-Depth-V2 MDE (middle) and ADE20k semantic segmentation (right).

Method	Backbone	crop size	mIoU $\uparrow$
SegFormer [53]	MiT-B5 [53]	512 <sup>2</sup>	51.0
Swin-UperNet [33, 52]	Swin-L [33]	640 <sup>2</sup>	52.1
ConvNeXt-UperNet [34, 52]	ConvNeXt-L [34]	640 <sup>2</sup>	52.1
ConvNeXt-UperNet [34, 52]	ConvNeXt-XL [34]	640 <sup>2</sup>	53.6
MaskFormer [10]	Swin-L [33]	640 <sup>2</sup>	54.1
DDP (step 3) [22]	Swin-L [33]	512 <sup>2</sup>	53.2
$\times$ ConvNeXt-L (ours)	Swin-L [33]	512 <sup>2</sup>	<b>54.3</b>

Table 7. Semantic segmentation performances on the ADE20k dataset.

Method	Backbone	mIoU (s.s.) $\uparrow$	mIoU (m.s.) $\uparrow$
Segmenter [47]	ViT-L [14]	79.10	81.30
SETR-PUP [62]	ViT-L [14]	79.34	82.15
StructToken [29]	ViT-L [14]	80.05	82.07
DDP (step 3) [22]	ConvNeXt-L [34]	83.21	83.92
DiversePatch [18]	Swin-L [33]	82.70	83.60
Mask2Former [11]	Swin-L [33]	83.30	84.30
$\times$ ConvNeXt-L (ours)	Swin-L [33]	<b>83.63</b>	<b>84.32</b>

Table 8. Semantic segmentation performances on the Cityscapes dataset. “s.s.” and “m.s.” denote single-scale and multi-scale inference results, respectively.

## 6.2. Qualitative analysis and efficiency comparison

As illustrated in Figure 5, and as mentioned in Subsection 5.2, pre-trained decoder predictions exhibit more robust semantic information compared to other methods, resulting in sharper and more coherent predictions. For instance, in the DDAD MDE predictions, Swin-L  $\times$  ConvNeXt-B demonstrates sharper detail than DepthFormer (GEA), maintaining precise contours for both large and small objects. In the DDAD MDE predictions, Metric3Dv2 is noted to cause some object deformations, whereas Swin-L  $\times$  ConvNeXt-L preserves accurate outlines. In the ADE20k semantic segmentation comparisons, DDP tends to show inconsistent errors in the central areas of large objects, yet Swin-L  $\times$  ConvNeXt-L maintains consistent predictions.

To ensure a fair comparison, we avoided performance

Model	Backbone	Dataset	FPS (image/s)
BinsFormer [28]	Swin-L [33]	NYU	2.20 <sup>†</sup>
NDDDepth [42]	Swin-L [33]	NYU	2.23 <sup>†</sup>
$\times$ ConvNeXtV2-T	Swin-L [33]	NYU	<b>5.21<sup>†</sup></b>
Depth Anything [55]	DINOv2-L [37]	NYU	1.85 <sup>†</sup>
Metric3Dv2 [20]	DINOv2-L [37]	NYU	0.89 <sup>†</sup>
$\times$ ConvNeXtV2-B	DINOv2-L [37]	NYU	<b>2.00<sup>†</sup></b>
BinsFormer [28]	Swin-L [33]	KITTI	1.70 <sup>†</sup>
NDDDepth [42]	Swin-L [33]	KITTI	1.82 <sup>†</sup>
$\times$ ConvNeXt-B	Swin-L [33]	KITTI	<b>3.32<sup>†</sup></b>
Depth Anything [55]	DINOv2-L [37]	KITTI	0.46 <sup>†</sup>
Metric3Dv2 [20]	DINOv2-L [37]	KITTI	0.63 <sup>†</sup>
$\times$ ConvNeXtV2-B	DINOv2-L [37]	KITTI	<b>1.33<sup>†</sup></b>
ConvNeXt-UperNet [34, 52]	ConvNeXt-XL [34]	ADE20K	13.97 <sup>‡</sup>
DDP [22]	Swin-L [33]	ADE20K	15.07 <sup>‡</sup>
$\times$ ConvNeXt-L	Swin-L [33]	ADE20K	<b>15.74<sup>‡</sup></b>
DDP [22]	Swin-L [33]	CityScapes	4.15 <sup>‡</sup>
$\times$ ConvNeXt-L	Swin-L [33]	CityScapes	<b>5.95<sup>‡</sup></b>

Table 9. Efficiency comparisons. <sup>†</sup> denotes FPS is evaluated on a RTX 2080 Super GPU, while <sup>‡</sup> denotes FPS is evaluated on a Tesla A100 GPU GPU, .

improvements that might arise from using computationally intensive decoders in the decoder section. Table 9 compares the computational efficiency of the primary competing methods, demonstrating that  $\times$ Net consistently maintains the highest efficiency across all comparisons.

## 7. Conclusion

This paper is the first to introduce the use of a pre-trained decoder in an encoder-decoder structure, termed  $\times$ Net. It achieves efficient dense prediction performance through the “pre-trained encoder  $\times$  pre-trained decoder” collaboration. The pre-trained decoder enriches the network’s intermediate features with semantic information, which improves the accuracy and the quality of details of dense predictions.



## References

- [1] Ashutosh Agarwal and Chetan Arora. Attention attention everywhere: Monocular depth prediction with skip attention. In *WACV*, pages 5861–5870, 2023. 7
- [2] Hangbo Bao, Li Dong, Songhao Piao, and Furu Wei. BEiT: BERT pre-training of image transformers. In *ICLR*, 2022. 2
- [3] Shariq Farooq Bhat, Ibraheem Alhashim, and Peter Wonka. Adabins: Depth estimation using adaptive bins. In *CVPR*, pages 4009–4018, 2021. 1, 2, 5
- [4] Shariq Farooq Bhat, Ibraheem Alhashim, and Peter Wonka. Localbins: Improving depth estimation by learning local distributions. In *ECCV*, pages 480–496. Springer, 2022. 2
- [5] Mathilde Caron, Hugo Touvron, Ishan Misra, Hervé Jégou, Julien Mairal, Piotr Bojanowski, and Armand Joulin. Emerging properties in self-supervised vision transformers. In *ICCV*, 2021. 2
- [6] Liang-Chieh Chen. Rethinking atrous convolution for semantic image segmentation. *arXiv preprint arXiv:1706.05587*, 2017. 2
- [7] Liang-Chieh Chen, George Papandreou, Iasonas Kokkinos, Kevin Murphy, and Alan L Yuille. Deeplab: Semantic image segmentation with deep convolutional nets, atrous convolution, and fully connected crfs. *IEEE TPAMI*, 40(4):834–848, 2017. 2
- [8] Liang-Chieh Chen, Yukun Zhu, George Papandreou, Florian Schroff, and Hartwig Adam. Encoder-decoder with atrous separable convolution for semantic image segmentation. In *ECCV*, pages 801–818, 2018. 2
- [9] Bowen Cheng, Maxwell D Collins, Yukun Zhu, Ting Liu, Thomas S Huang, Hartwig Adam, and Liang-Chieh Chen. Panoptic-deeplab: A simple, strong, and fast baseline for bottom-up panoptic segmentation. In *CVPR*, pages 12475–12485, 2020. 2
- [10] Bowen Cheng, Alex Schwing, and Alexander Kirillov. Per-pixel classification is not all you need for semantic segmentation. *NeurIPS*, 34:17864–17875, 2021. 2, 8
- [11] Bowen Cheng, Ishan Misra, Alexander G Schwing, Alexander Kirillov, and Rohit Girdhar. Masked-attention mask transformer for universal image segmentation. In *CVPR*, pages 1290–1299, 2022. 2, 7, 8
- [12] MMSegmentation Contributors. MMSegmentation: Openmmlab semantic segmentation toolbox and benchmark. <https://github.com/open-mmlab/mms Segmentation>, 2020. 5
- [13] Marius Cordts, Mohamed Omran, Sebastian Ramos, Timo Rehfeld, Markus Enzweiler, Rodrigo Benenson, Uwe Franke, Stefan Roth, and Bernt Schiele. The cityscapes dataset for semantic urban scene understanding. In *CVPR*, pages 3213–3223, 2016. 5
- [14] Alexey Dosovitskiy, Lucas Beyer, Alexander Kolesnikov, Dirk Weissenborn, Xiaohua Zhai, Thomas Unterthiner, Mostafa Dehghani, Matthias Minderer, Georg Heigold, Sylvain Gelly, Jakob Uszkoreit, and Neil Houlsby. An image is worth 16x16 words: Transformers for image recognition at scale. *ICLR*, 2021. 8
- [15] Stefan Elfving, Eiji Uchibe, and Kenji Doya. Sigmoid-weighted linear units for neural network function approximation in reinforcement learning. *Neural networks*, 107:3–11, 2018.
- [16] Andreas Geiger, Philip Lenz, Christoph Stiller, and Raquel Urtasun. Vision meets robotics: The kitti dataset. *The International Journal of Robotics Research*, 32(11):1231–1237, 2013. 5
- [17] Clément Godard, Oisín Mac Aodha, and Gabriel J Brostow. Unsupervised monocular depth estimation with left-right consistency. In *CVPR*, pages 270–279, 2017. 1
- [18] Chengyue Gong, Dilin Wang, Meng Li, Vikas Chandra, and Qiang Liu. Vision transformers with patch diversification. *arXiv preprint arXiv:2104.12753*, 2021. 8
- [19] Vitor Guizilini, Rares Ambrus, Sudeep Pillai, Allan Ravenstos, and Adrien Gaidon. 3d packing for self-supervised monocular depth estimation. In *CVPR*, pages 2485–2494, 2020. 5
- [20] Mu Hu, Wei Yin, Chi Zhang, Zhipeng Cai, Xiaoxiao Long, Hao Chen, Kaixuan Wang, Gang Yu, Chunhua Shen, and Shaojie Shen. Metric3d v2: A versatile monocular geometric foundation model for zero-shot metric depth and surface normal estimation. *arXiv preprint arXiv:2404.15506*, 2024. 1, 7, 8
- [21] Zilong Huang, Xinggang Wang, Lichao Huang, Chang Huang, Yunchao Wei, and Wenyu Liu. Ccnet: Criss-cross attention for semantic segmentation. In *ICCV*, pages 603–612, 2019. 2
- [22] Yuanfeng Ji, Zhe Chen, Enze Xie, Lanqing Hong, Xihui Liu, Zhaoqiang Liu, Tong Lu, Zhenguo Li, and Ping Luo. Ddp: Diffusion model for dense visual prediction. In *ICCV*, pages 21741–21752, 2023. 4, 7, 8
- [23] Alexander Kirillov, Evgeny Levinkov, Bjoern Andres, Bogdan Savchynskyy, and Carsten Rother. Instancecut: from edges to instances with multicut. In *CVPR*, pages 5008–5017, 2017. 2
- [24] Alexander Kirillov, Ross Girshick, Kaiming He, and Piotr Dollár. Panoptic feature pyramid networks. In *CVPR*, pages 6399–6408, 2019. 2
- [25] Alexander Kirillov, Eric Mintun, Nikhila Ravi, Hanzi Mao, Chloe Rolland, Laura Gustafson, Tete Xiao, Spencer Whitehead, Alexander C Berg, Wan-Yen Lo, et al. Segment anything. In *ICCV*, pages 4015–4026, 2023. 1
- [26] Jin Han Lee, Myung-Kyu Han, Dong Wook Ko, and Il Hong Suh. From big to small: Multi-scale local planar guidance for monocular depth estimation. *arXiv preprint arXiv:1907.10326*, 2019. 1
- [27] Zhenyu Li, Zehui Chen, Xianming Liu, and Junjun Jiang. Depthformer: Exploiting long-range correlation and local information for accurate monocular depth estimation. *Machine Intelligence Research*, 20(6):837–854, 2023. 7
- [28] Zhenyu Li, Xuyang Wang, Xianming Liu, and Junjun Jiang. Binsformer: Revisiting adaptive bins for monocular depth estimation. *IEEE TIP*, 2024. 2, 5, 7, 8
- [29] Fangjian Lin, Zhanhao Liang, Sitong Wu, Junjun He, Kai Chen, and Shengwei Tian. Structtoken: Rethinking semantic segmentation with structural prior. *IEEE TCSVT*, 33(10):5655–5663, 2023. 8

- [30] Guosheng Lin, Anton Milan, Chunhua Shen, and Ian Reid. Refinenet: Multi-path refinement networks for high-resolution semantic segmentation. In *CVPR*, pages 1925–1934, 2017. 1
- [31] Tsung-Yi Lin, Piotr Dollár, Ross Girshick, Kaiming He, Bharath Hariharan, and Serge Belongie. Feature pyramid networks for object detection. In *CVPR*, pages 2117–2125, 2017. 2
- [32] Ce Liu, Suryansh Kumar, Shuhang Gu, Radu Timofte, and Luc Van Gool. Single image depth prediction made better: A multivariate gaussian take. In *CVPR*, pages 17346–17356, 2023. 7
- [33] Ze Liu, Yutong Lin, Yue Cao, Han Hu, Yixuan Wei, Zheng Zhang, Stephen Lin, and Baining Guo. Swin transformer: Hierarchical vision transformer using shifted windows. In *ICCV*, pages 10012–10022, 2021. 5, 7, 8
- [34] Zhuang Liu, Hanzi Mao, Chao-Yuan Wu, Christoph Feichtenhofer, Trevor Darrell, and Saining Xie. A convnet for the 2020s. In *Proceedings of the IEEE/CVF conference on computer vision and pattern recognition*, pages 11976–11986, 2022. 5, 7, 8
- [35] Jonathan Long, Evan Shelhamer, and Trevor Darrell. Fully convolutional networks for semantic segmentation. In *CVPR*, pages 3431–3440, 2015. 1, 2
- [36] Nikolaus Mayer, Eddy Ilg, Philip Hausser, Philipp Fischer, Daniel Cremers, Alexey Dosovitskiy, and Thomas Brox. A large dataset to train convolutional networks for disparity, optical flow, and scene flow estimation. In *CVPR*, pages 4040–4048, 2016. 1
- [37] Maxime Oquab, Timothée Darcet, Théo Moutakanni, Huy Vo, Marc Szafraniec, Vasil Khalidov, Pierre Fernandez, Daniel Haziza, Francisco Massa, Alaaeldin El-Nouby, et al. Dinov2: Learning robust visual features without supervision. *arXiv preprint arXiv:2304.07193*, 2023. 1, 2, 7, 8
- [38] Luigi Piccinelli, Yung-Hsu Yang, Christos Sakaridis, Mattia Segu, Siyuan Li, Luc Van Gool, and Fisher Yu. Unidepth: Universal monocular metric depth estimation. In *CVPR*, pages 10106–10116, 2024. 7
- [39] Alec Radford, Jong Wook Kim, Chris Hallacy, Aditya Ramesh, Gabriel Goh, Sandhini Agarwal, Girish Sastry, Amanda Askell, Pamela Mishkin, Jack Clark, et al. Learning transferable visual models from natural language supervision. In *International conference on machine learning*, pages 8748–8763. PMLR, 2021. 2
- [40] René Ranftl, Alexey Bochkovskiy, and Vladlen Koltun. Vision transformers for dense prediction. In *CVPR*, pages 12179–12188, 2021. 1, 2, 4
- [41] Olga Russakovsky, Jia Deng, Hao Su, Jonathan Krause, Sanjeev Satheesh, Sean Ma, Zhiheng Huang, Andrej Karpathy, Aditya Khosla, Michael Bernstein, et al. Imagenet large scale visual recognition challenge. *International journal of computer vision*, 115:211–252, 2015. 2
- [42] Shuwei Shao, Zhongcai Pei, Weihai Chen, Xingming Wu, and Zhengguo Li. Ndddepth: Normal-distance assisted monocular depth estimation. In *ICCV*, pages 7931–7940, 2023. 1, 2, 5, 7, 8
- [43] Shuwei Shao, Zhongcai Pei, Xingming Wu, Zhong Liu, Weihai Chen, and Zhengguo Li. Iebins: Iterative elastic bins for monocular depth estimation. *NeurIPS*, 36, 2024. 2
- [44] Wenzhe Shi, Jose Caballero, Ferenc Huszár, Johannes Totz, Andrew P Aitken, Rob Bishop, Daniel Rueckert, and Zehan Wang. Real-time single image and video super-resolution using an efficient sub-pixel convolutional neural network. In *CVPR*, pages 1874–1883, 2016. 3
- [45] Nathan Silberman, Derek Hoiem, Pushmeet Kohli, and Rob Fergus. Indoor segmentation and support inference from rgbd images. In *ECCV*, pages 746–760. Springer, 2012. 5
- [46] Shuran Song, Samuel P Lichtenberg, and Jianxiong Xiao. Sun rgb-d: A rgb-d scene understanding benchmark suite. In *CVPR*, pages 567–576, 2015. 5
- [47] Robin Strudel, Ricardo Garcia, Ivan Laptev, and Cordelia Schmid. Segmenter: Transformer for semantic segmentation. In *ICCV*, pages 7262–7272, 2021. 8
- [48] Chen Sun, Abhinav Shrivastava, Saurabh Singh, and Abhinav Gupta. Revisiting unreasonable effectiveness of data in deep learning era. In *Proceedings of the IEEE international conference on computer vision*, pages 843–852, 2017. 1
- [49] Xiaolong Wang, Ross Girshick, Abhinav Gupta, and Kaiming He. Non-local neural networks. In *CVPR*, pages 7794–7803, 2018. 2
- [50] Philippe Weinzaepfel, Thomas Lucas, Vincent Leroy, Johann Cabon, Vaibhav Arora, Romain Brégier, Gabriela Csurka, Leonid Antsfeld, Boris Chidlovskii, and Jérôme Revaud. Croco v2: Improved cross-view completion pre-training for stereo matching and optical flow. In *ICCV*, pages 17969–17980, 2023. 1
- [51] Sanghyun Woo, Shoubhik Debnath, Ronghang Hu, Xinlei Chen, Zhuang Liu, In So Kweon, and Saining Xie. Convnext v2: Co-designing and scaling convnets with masked autoencoders. In *CVPR*, pages 16133–16142, 2023. 7
- [52] Tete Xiao, Yingcheng Liu, Bolei Zhou, Yuning Jiang, and Jian Sun. Unified perceptual parsing for scene understanding. In *ECCV*, pages 418–434, 2018. 1, 8
- [53] Enze Xie, Wenhai Wang, Zhiding Yu, Anima Anandkumar, Jose M Alvarez, and Ping Luo. Segformer: Simple and efficient design for semantic segmentation with transformers. *NeurIPS*, 34:12077–12090, 2021. 8
- [54] Haofei Xu, Jing Zhang, Jianfei Cai, Hamid Rezaatofighi, Fisher Yu, Dacheng Tao, and Andreas Geiger. Unifying flow, stereo and depth estimation. *IEEE TPAMI*, 2023. 1
- [55] Lihe Yang, Bingyi Kang, Zilong Huang, Xiaogang Xu, Jiashi Feng, and Hengshuang Zhao. Depth anything: Unleashing the power of large-scale unlabeled data. In *CVPR*, pages 10371–10381, 2024. 1, 7, 8
- [56] Xiaodong Yang, Zhuang Ma, Zhiyu Ji, and Zhe Ren. Gedepth: Ground embedding for monocular depth estimation. In *ICCV*, pages 12719–12727, 2023. 2, 5, 7
- [57] Weihao Yuan, Xiaodong Gu, Zuozhuo Dai, Siyu Zhu, and Ping Tan. Neural window fully-connected crfs for monocular depth estimation. In *CVPR*, pages 3916–3925, 2022. 2
- [58] Weihao Yuan, Xiaodong Gu, Zuozhuo Dai, Siyu Zhu, and Ping Tan. Newcrfs: Neural window fully-connected crfs for monocular depth estimation. In *CVPR*, 2022. 5, 7

- [59] Biao Zhang and Rico Sennrich. Root mean square layer normalization. *NeurIPS*, 32, 2019.
- [60] Hengshuang Zhao, Jianping Shi, Xiaojuan Qi, Xiaogang Wang, and Jiaya Jia. Pyramid scene parsing network. In *CVPR*, pages 2881–2890, 2017. [2](#)
- [61] Hengshuang Zhao, Jianping Shi, Xiaojuan Qi, Xiaogang Wang, and Jiaya Jia. Pyramid scene parsing network. In *CVPR*, pages 2881–2890, 2017. [1](#), [2](#)
- [62] Sixiao Zheng, Jiachen Lu, Hengshuang Zhao, Xiatian Zhu, Zekun Luo, Yabiao Wang, Yanwei Fu, Jianfeng Feng, Tao Xiang, Philip HS Torr, et al. Rethinking semantic segmentation from a sequence-to-sequence perspective with transformers. In *CVPR*, pages 6881–6890, 2021. [8](#)
- [63] Bolei Zhou, Hang Zhao, Xavier Puig, Sanja Fidler, Adela Barriuso, and Antonio Torralba. Scene parsing through ade20k dataset. In *CVPR*, pages 633–641, 2017. [5](#)

# Supplementary file for Is Pre-training Applicable to the Decoder for Dense Prediction?

Anonymous ICCV submission

Paper ID 7464

arXiv:2503.07637v1 [cs.LG] 5 Mar 2025

## A. Experiment settings

**Our code will be released.** Detailed training specifications are provided in our repository.

**NYU-Depth-V2 and KITTI training.** We employ the AdamW optimizer with an initial learning rate of  $1 \times 10^{-6}$ , a weight decay of 0.01, a scheduler that uses linear learning rate decay, and a linear warmup of 1,600 iterations. Models are trained on 8 GPUs with 2 images per GPU for 80K iterations. Additionally, the learning rate for the Swin-L encoder is multiplied by 0.1, while for the DINOv2-L encoder, it is multiplied by 0.01. For augmentations, we follow previous works by simply employing random rotations, random flips, and color augmentation.

**DDAD training.** We use the AdamW optimizer with an initial learning rate of  $1 \times 10^{-6}$ , a weight decay of 0.01, and a linear learning rate decay scheduler with a 1,600-iteration warmup. The Swin-L encoder’s learning rate is scaled by 0.1. Training occurs on 8 GPUs with 2 images per GPU over 120K iterations. For augmentations, we follow the approach of GEDepth [? ].

**ADE20k and CityScapes training.** We employ the AdamW optimizer with an initial learning rate of  $2.5 \times 10^{-4}$ , a weight decay of 0.01, a scheduler that uses linear learning rate decay, and a linear warmup of 1,500 iterations. Models are trained on 8 GPUs with 2 images per GPU for 160K iterations. For augmentations, we adopt the default setting introduced in [? ] of random horizontal flipping, random re-scaling within ratio range [0.5, 2.0] and random photometric distortion.

## B. Metrics

**Monocular depth estimation metrics.** Following established protocols [? ? ? ], we evaluate our monocular depth estimation models using standard metrics: absolute relative error (Abs Rel), root mean squared error (RMSE), log10 error (log10), root mean squared error in log space (RMS\_log), and accuracy under threshold of 1.25 ( $\delta < 1.25$ ). For KITTI online validation, we used the official KITTI metrics.

**Semantic segmentation metrics.** Average accuracy (aAcc), mean accuracy (mAcc), and mean Intersection over Union (mIoU) are used in our paper. For multi-scale inference, we employed the standard six scales: [0.5, 0.75, 1.0, 1.25, 1.5, 1.75].

## C. Qualitative comparison

We conducted qualitative comparisons on NYU Depth-V2, DDAD, and ADE20K datasets, with the results illustrated in Figures 1, 2, and 3, respectively. As can be clearly observed from the numerous comparative results in Figures 1 and 2,  $\times$ Net exhibits more refined predictive details, consistent with the analysis in Section 4 of the paper. The pre-trained decoder enriches the semantic information in the intermediate feature maps, resulting in sharper object boundaries and details. Additionally, the results in Figure 3 demonstrate that the pre-trained decoder achieves greater continuity in predictions compared to other methods.

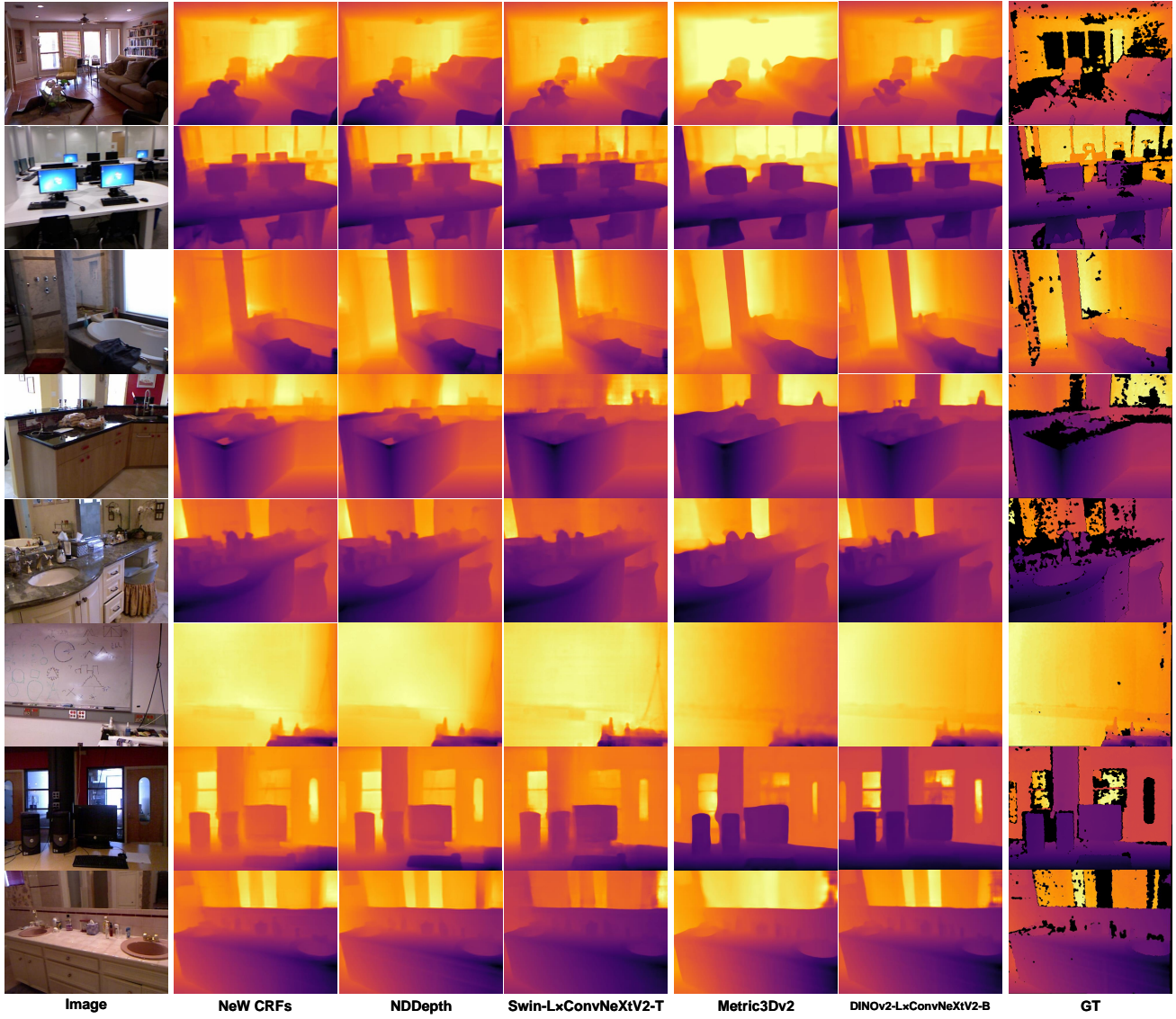


Figure 1. Qualitative comparison on NYU Depth-V2 monocular depth estimation. Since the fine-tuned model of Metric3Dv2 on NYU-Depth-V2 has not been released, the Metric3Dv2 model used here is the zero-shot model.

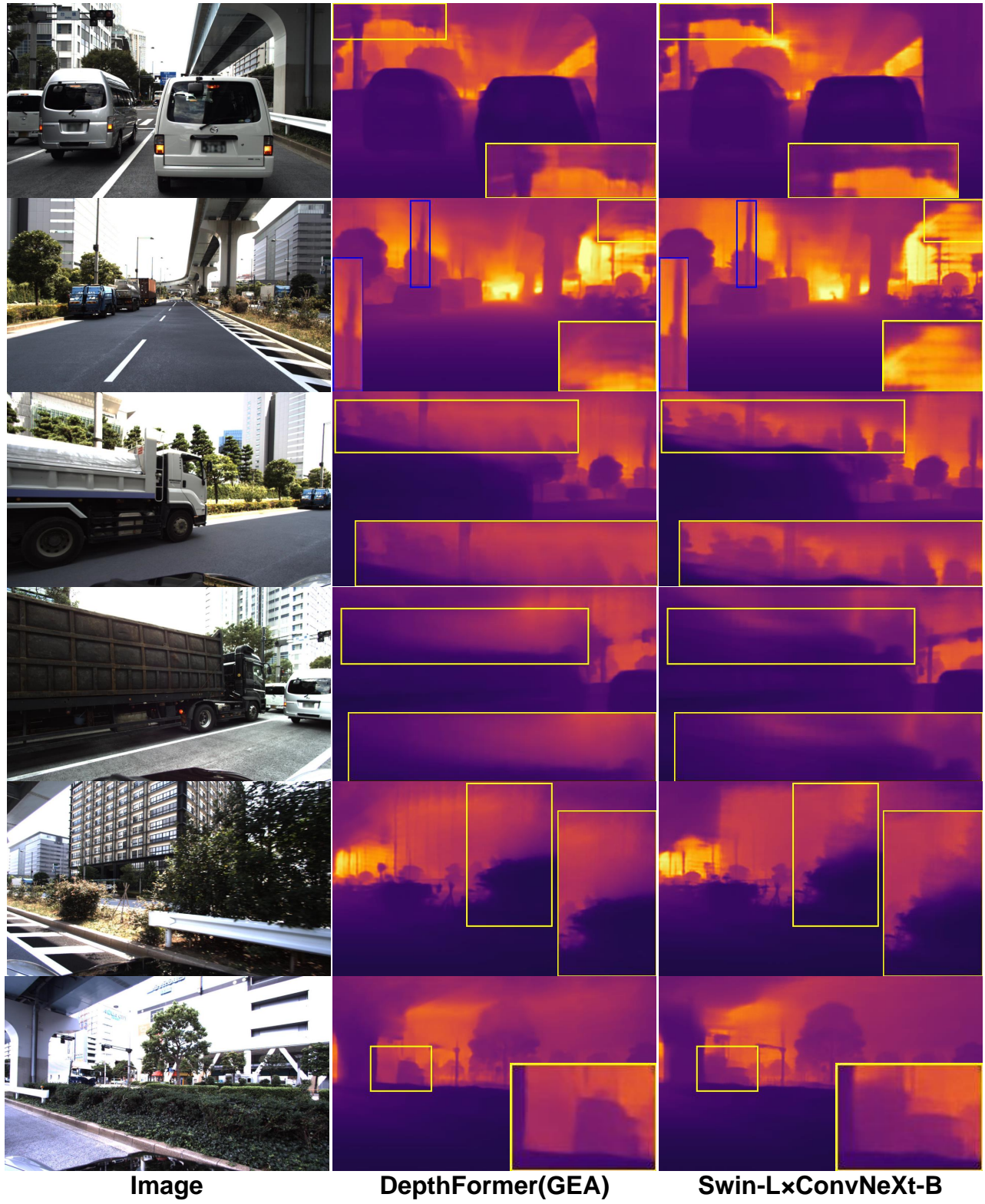


Figure 2. Qualitative comparison on DDAD monocular depth estimation.

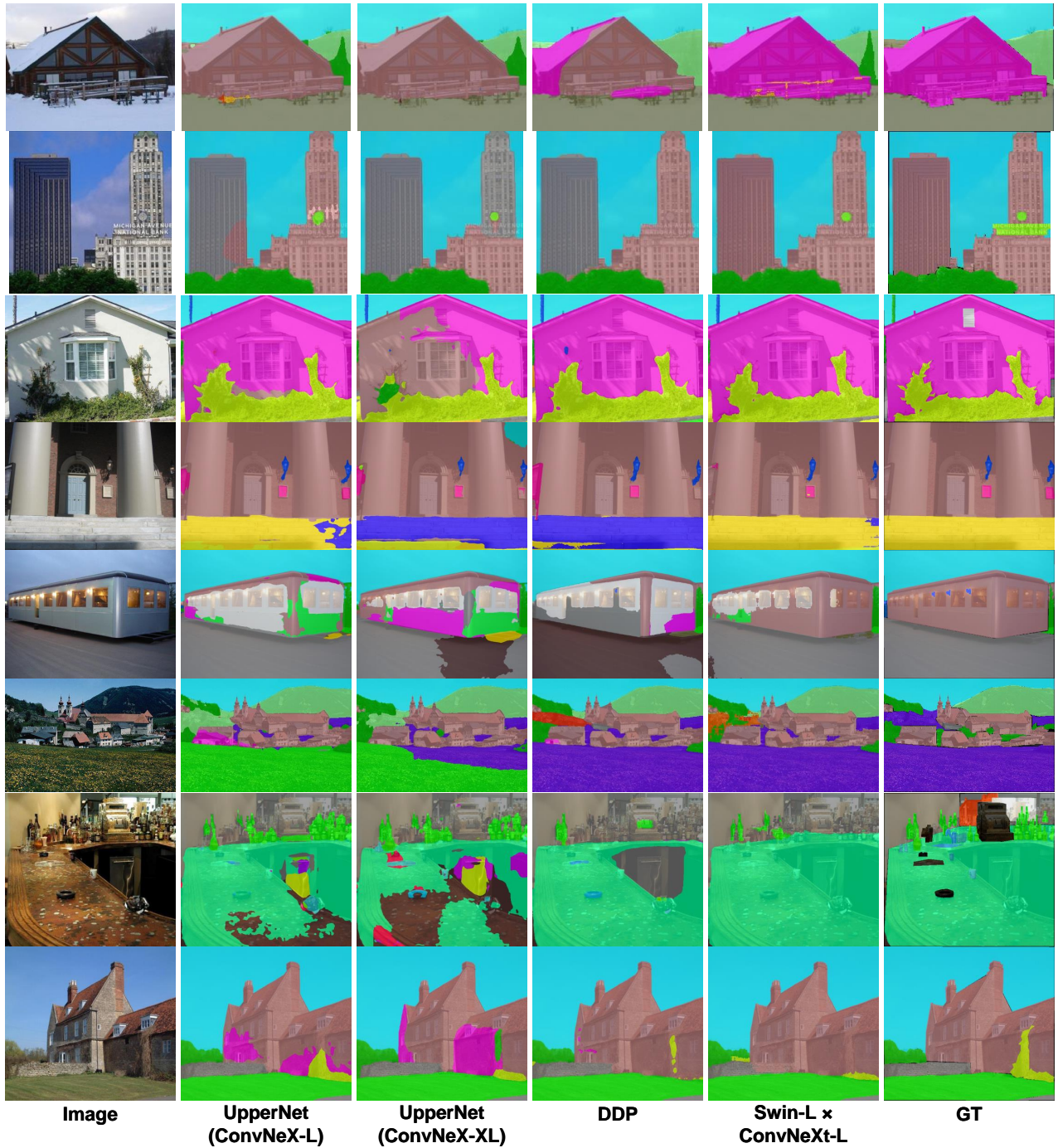


Figure 3. Qualitative comparison on ADE20K semantic segmentation.